International Journal of Coal Geology 279 (2023) 104373

Contents lists available at ScienceDirect

International Journal of Coal Geology

journal homepage: www.elsevier.com/locate/coal

The effect of lamina and lithofacies assemblage on molecular maturity of oil in a shale source-rock reservoir

Weijiao Ma [a,b], Yingchang Cao [b,*], Kelai Xi [b], Miruo Lin [b], Jinzhong Liu [a], Yunpeng Wang [a,*]

[a] State Key Laboratory of Organic Geochemistry, Guangzhou Institute of Geochemistry, Chinese Academy of Sciences, Guangzhou 510640, China
[b] National Key Laboratory of Deep Oil and Gas, China University of Petroleum (East China), Qingdao 266580, China

ARTICLE INFO

Keywords:
Hybrid shale system
Lithofacies assemblage
Hydrocarbon expulsion
Molecular composition
Molecular thermal maturity

ABSTRACT

This paper discusses the effect of the source rock–reservoir assemblage and the assemblage–induced variability in hydrocarbon expulsion and the subsequent molecular composition as well as molecular thermal maturity within a hybrid shale system. The characterization work was conducted on lithofacies and microlamina scales using core samples from the Chang 7_3 sub-member of the Triassic Yanchang Formation in the Ordos Basin, China. Samples were collected from a narrow interval with a depth range of less than 15 m, and the main characterization work was performed by Rock-Eval pyrolysis and GC–MS analysis. The results show that chemical fractionation of preferential expulsion and migration of the saturated fraction exists in the source rock–reservoir assemblages at both the lithofacies and lamina scales. However, the molecular composition behaves differently at the lithofacies and lamina scale's source rock–reservoir assemblages, in which $\sum C_{21-}/\sum C_{22+}$ is higher in lamina scale reservoir but lower in lithofacies scale reservoir. It is assumed that the low-molecular weight *n*-alkanes also follow molecular fractionation. The lithofacies reservoir has a lower $\sum C_{21-}/\sum C_{22+}$ because of the strong storage capacity of the laminated micro-reservoir within shale, which prevents the newly generated lighter oil from being charged into the lithofacies reservoir. The variation trends of thermal maturity indices Ts/hopane, the relative pregnane content, and TA(I)/TA(I + II) ratios, which have the same chemical basis with $\sum C_{21-}/\sum C_{22+}$, carry the same maturity signature as $\sum C_{21-}/\sum C_{22+}$. The above profile of the molecular composition and molecular-derived thermal maturity parameters indicate that within the short interval of a shale system where no differences in thermal maturity are expected, chain scission reactions and their derived thermal maturity indicators are very sensitive to source rock and reservoir. In addition, within a shale system, oil is more easily to expel out from the organic-rich lithofacies that are interbedded with organic-lean lithofacies. Oil expulsion may promote both chain cracking of oil and subsequently kerogen decomposition. This may provide geological evidence to explain why the frequent-stacking assemblage of source rock and reservoir lithofacies in a hybrid shale system is an ideal target for shale oil exploration.

1. Introduction

Thermal maturity is an indispensable factor used to evaluate the hydrocarbon generation capacity and shale oil producibility of unconventional source-rock reservoirs. If the source rock contains vitrinite, vitrinite reflectance measurement is undoubtedly the most appropriate method to assess thermal maturity. Although not as common as vitrinite, reflectance of other macerals (such as graptolite, chitinozoan, and spore) and kerogen transformation products (pyro-) bitumen are alternative components that can be used to obtain maturity features (e.g., Hackley and Cardott, 2016; Peterson et al., 2020). In addition to petrographic approaches, numerical method like basin modelling (e.g., Rodon and Littke, 2005), geochemical methods such as Rock-Eval pyrolysis (e.g., Tissot et al., 1987; Jarvie et al., 2001) and gas chromatography–mass spectrometry (GC–MS) (e.g., Peters et al., 2005) are also secondary options. Apart from such methods, solid state spectroscopic methods, such as Raman spectroscopy (e.g., Jubb et al., 2018; Henry et al., 2019), Fourier transformation infrared spectroscopy (FT-IR) (e.g., Lis et al., 2005; Chen et al., 2012), and ^{13}C nuclear magnetic resonance (^{13}C NMR) (e.g., Kelemen et al., 2007; Mao et al., 2010) can be used to investigate chemical changes in the structure of organic matter and thus to track thermal maturation. Numerous vitrinite reflectance equivalent thermal

* Corresponding authors.
E-mail addresses: caoych@upc.edu.cn (Y. Cao), wangyp@gig.ac.cn (Y. Wang).

https://doi.org/10.1016/j.coal.2023.104373
Received 29 May 2023; Received in revised form 14 September 2023; Accepted 4 October 2023
Available online 5 October 2023

maturity parameters can be calculated from the T_{max} of Rock-Eval pyrolysis, (non-) biological makers in GC–MS, and relative concentrations between aliphatic and/or aromatic signals in Raman spectroscopy, FT-IR, and ^{13}C NMR (e.g., Radke et al., 1982; Jarvie et al., 2001; Lis et al., 2005; Mao et al., 2010; Hackley and Lünsdorf, 2018). In this respect, Rock-Eval pyrolysis and GC–MS are extensively applied, owing to their efficient, reproducible, and less labor-intensive characteristics.

Heterogeneity creates difficulties when assessing thermal maturity in shale systems, due to the lateral and vertical frequent variations in organic matter richness, the mineralogy, and the stratigraphic fabric. In a typical shale source-rock reservoir, the organic-rich source rock (usually shale) and organic-lean reservoir lithofacies (such as carbonate, sandstone, and siltstone) are often juxtaposed (overlying, underlying, or interbedded) (Jarvie, 2012). Within individual organic-rich lithofacies, the lamina of finer grains rich in organic matter are usually interspersed with lamina of coarser grains that contain less organic matter, and this results in various stacking styles (such as parallel, wavy, and lenticular) (Knapp et al., 2017; Yawar and Schieber, 2017; Chukwuma et al., 2021). At lithofacies scale, oils can be expelled from shale into the interbedded sandstone, while at lamina scale, oils generated by organic-rich lamina are more easily drained to the interlaminated organic-lean silty lamina (Jarvie, 2012b; Ma et al., 2022). The heavy fractions of migrated oil in the interbedded sandstone and interlaminated silty lamina are not always readily vaporized at 300 °C, which results in the production of a measurable signal in the low temperature range of the S_2 peak, leading to suppressed T_{max} values (Espitalié et al., 1977; Clementz, 1979; King et al., 2015). Numerous studies have reported the effects of oil expulsion or retention within hybrid shale system on T_{max} as an indicator of thermal maturity (Jarvie, 2012; Han et al., 2015; Li et al., 2018). For example, the case study of Li et al. (2018) focused on the Eocene-Oligocene Qianjiang Formation (Jianghan Basin, China) and the results indicated that the presence of large amounts of expelled oil in beds with larger pore spaces resulted in a low T_{max} value. Another example relates to the 2_{nd} interval of Barnett Shale (Carboniferous, USA), which is rich in quartz, lean in organic matter, and receives hydrocarbons from the adjacent organic-rich intervals; a ΔT_{max} value greater than 10 °C was reported before and after the rocks were solvent extracted (Han et al., 2015). However, petroleum geochemist rarely measures rock powder from lamina scale. Rock powder usually made up of centimeter scale core or even cutting chips, which would inevitably mask some micro-scale geochemical signatures.

In the present study, we mainly focused on the spatial variations of the bulk and molecular compositions in a self-sourced and self-reserved shale system. Our main objective was to investigate the influences of the

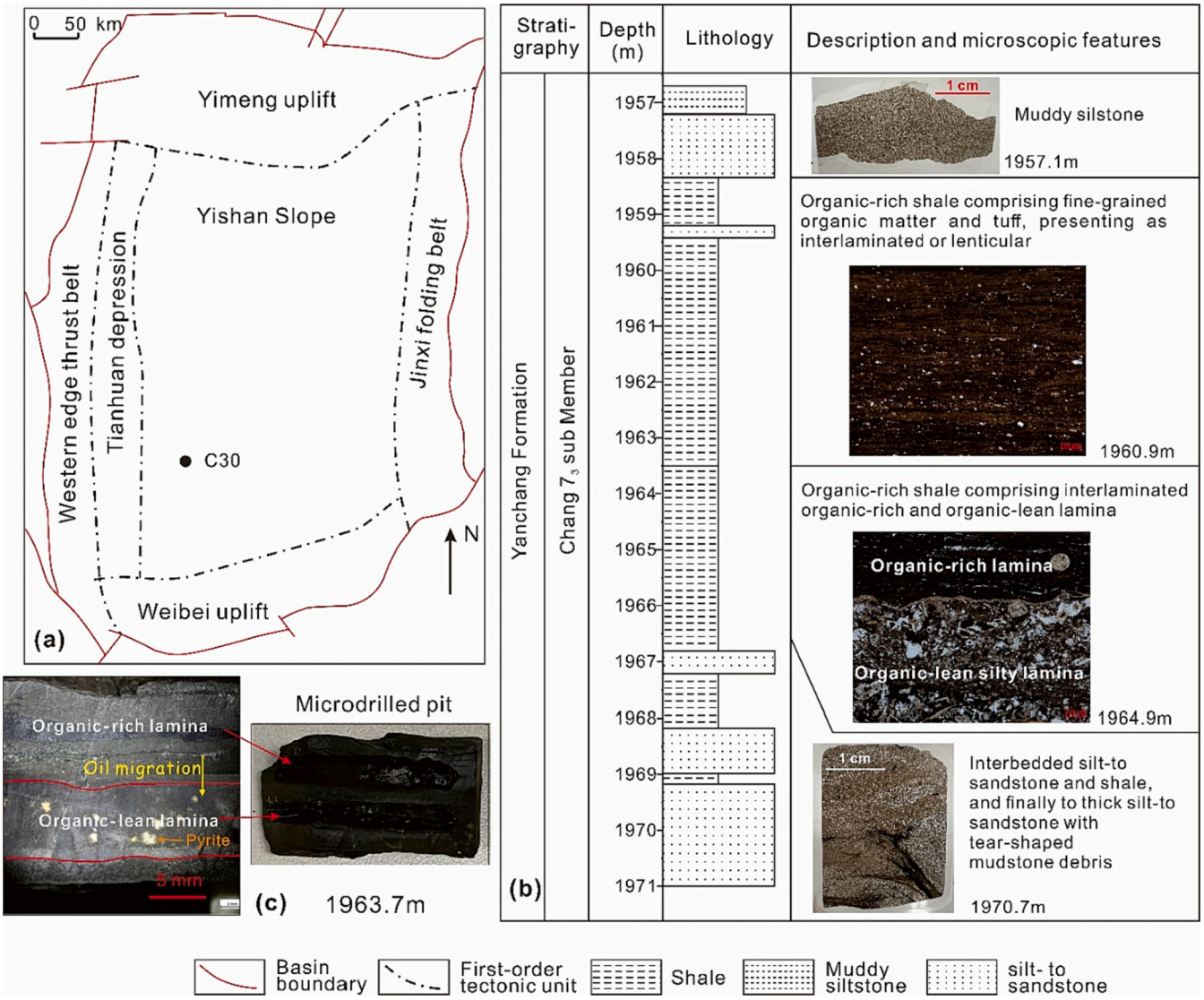

Fig. 1. (a) Simplified tectonic units of the Ordos Basin and location of the studied well C30 (marked with black solid circles). (b) Lithological features and lamina distribution of the studied well. (c) A piece of shale (1963.7 m) selected for microdrilling.

lamina and the lithofacies assemblage on the (non-) biological molecular composition as well as molecular-derived thermal maturity indicators of shale oil.

2. Geological background and sample set

2.1. Geological background and sample set

The study area was the seventh member of the Triassic Yanchang Formation (Chang 7 shale) in the Ordos Basin, China (Fig. 1a). The basic lithologic characteristic for Chang 7 shale oil system is hybrid system with a combination of juxtaposed organic-rich and organic-lean intervals. The word "sandwiched" is specifically used to describe the stacked siltstone and mudrocks lithologies in the Chang 7_3 sub-member. Core samples were collected from the Chang 7_3 sub-member of the C30 well in the southern part of the basin. The Chang 7_3 sub-member of the C30 well mainly comprises thick layers of deep to semi-deep lacustrine shale interbedded with thin layers of deep-water gravity flow siltstone or sandstone (Zou et al., 2012). In the upper interval of the thick shale layer, the sediments mainly comprise fine-grained organic matter and tuff presenting as interlaminated or lenticular. The silt-sized deposits increase with depth, and these mainly comprise long strips of detrital K-feldspar or sharply angular detrital K-feldspar. In the lower interval of the thick shale layer, coarser grain-sized lamina with thicknesses of even centimeter is developed within the shale lithofacies. For convenience, this work uses previously defined nomenclature and refers to the fine-grained deposits in shale as organic-rich lamina and the silt-sized deposits in shale as silty lamina (Ma et al., 2022). Further down, the lithofacies become thin layers of interbedded silt-to sandstone and shale, and finally to thick silt-to sandstone with tear-shaped mudstone debris (Fig. 1b).

Twelve samples were used for analysis, including two samples from the uppermost and the lowermost muddy siltstone and siltstone, four shales samples mainly comprising organic-rich lamina, three shale samples enriched with silty lamina, and three interbedded siltstones (Table 1). The sample set covered a narrow depth range of less than 15 m. Although a 15-m interval is such a small interval and it's like a micro-environment, considering the basic cyclic overlapping lithologic features of sandstone and shale, the basic unit can be extrapolated to a larger interval. To reveal the generation and expulsion features on a microlamina-scale, one shale with thick and well-defined lamina was selected and microdrilled to separate the organic-rich lamina from the organic-lean lamina (Fig. 1c). The detailed microdrilling process used is provided in Ma et al. (2022).

2.2. Analytical procedure

All rock samples were pulverized in preparation for solvent extraction and pyrolysis analysis. Extractable organic matter (EOM) for rock samples was obtained by an accelerated solvent extractor (ASE, Dionex ASE-200) using dichloromethane (DCM)/methanol (93:7, v:v) as the solvent. The ASE was operated at 1500 psi and at 120 °C by first preheating for 5 min and then flushing with 80 mL of solvent for 10 min. For the microdrilled samples, due to limited sample quantity, the EOM was obtained via ultrasonic extract using the same organic solvent as that used for rock samples. After mass quantification, approximately 20–30 mg of the rock extracts and all the microdrilled sample extracts were prepared for group component separation. Asphaltenes were firstly precipitated by excess petroleum ether, and the remaining fractions were then separated using a silica gel (80–100 mesh)-alumina (100–200 mesh) (1:3, w:w) chromatography column. Petroleum ether was employed to elute the saturates, followed by petroleum ether/DCM (1:2, v:v) to isolate the aromatics, and finally DCM was used to obtain the resins.

GC–MS analysis of the saturated and aromatic fractions were performed on an Agilent 8890 gas chromatograph coupled with a 5977B mass spectrometer. The GC was equipped with a HP-5MS fused silica capillary column (30 m × 250 μm i.d. × 0.25 μm film thickness). The programmed temperature for GC oven was maintained at 50 °C for 2 min, ramped to 300 °C at 3 °C/min, and finally held for 10 min. Helium was used as the carrier gas at a constant of 1 mL/min. The analysis was conducted using selective ion monitoring mode.

Both the extracted and unextracted rock and microdrilled samples were subjected to pyrolysis using a Rock-Eval 7 VINCI instrument. According to the organic richness of the samples, between 5 mg and 40 mg of powder was loaded to prevent saturation of the flame ionization detector (FID) and infrared (IR) detectors. For pyrolysis, the temperature program started isothermally at 300 °C and held for 3 min to yield free hydrocarbons S_1, and subsequently increased to 650 °C at a heating rate of 25 °C/min to yield residual hydrocarbon potential S_2. TOC data are also obtained from Rock-Eval pyrolysis (refer to Behar et al., 2001 for details).

Table 1
Sample description, concentrations of extractable organic matter (EOM), relative proportions of group components in EOM, and Rock-Eval parameters of the unextracted and extracted rocks.

Sample depth (m)	Description	Extracted bitumen				Rock-Eval pyrolysis of unextracted samples						Rock-Eval pyrolysis of extracted samples				
		EOM	Sat	Aro	S/A	S_1	S_2	TOC	Tmax	HI	S_1/TOC	S_1'	S_2'	TOC′	Tmax’	HI’
		(mg/g TOC)	(%)	(%)	–	(mg/g)	(mg/g)	(wt %)	(°C)	(mg/g)	(mg/g TOC)	(mg/g)	(mg/g)	(wt %)	(°C)	(mg/g)
1957.6	Muddy siltstone	669.2	62.5	13.8	4.54	3.91	5.78	1.45	422	399	269.7	0.04	0.81	0.69	454	117
1960.9	Shale	61.2	25.0	23.1	1.08	3.15	23.79	12.37	442	192	25.5	0.08	21.14	13.18	440	160
1961.5	Shale	95.6	34.2	19.8	1.73	1.53	12.75	6.73	444	189	22.7	0.04	9.89	7.19	445	138
1963.7	Shale	109.9	31.9	21.8	1.46	4.71	30.07	14.01	442	215	33.6	0.07	21.97	14.58	445	151
1964.9	Shale	85.5	30.0	22.5	1.33	4.52	27.03	13.65	443	198	33.1	0.09	22.31	14.28	445	156
1966.5	Shale	61.8	19.3	23.1	0.83	6.04	46.64	26.28	441	177	23.0	0.3	43.94	28.44	443	155
1966.9	Shale mixed with siltstone	330.0	46.3	13.7	3.37	3.83	22.39	5.28	439	424	72.5	0.09	6.47	3.66	446	177
1967.7	Shale	65.4	26.3	23.6	1.12	6.81	46.44	24.77	443	187	27.5	0.3	41.41	25.54	443	162
1968.9	Siltstone	488.9	54.0	12.4	4.35	2.58	4.13	1.45	431	285	177.9	0.02	0.83	0.87	449	95
1969.2	Shale	78.9	24.3	26.1	0.93	6.92	40.15	19.49	444	206	35.5	0.15	35.83	21.47	445	167
1969.8	Sandstone	520.2	61.2	11.4	5.38	3.05	3.51	1.26	420	279	242.1	0.02	0.48	0.68	446	71
1970.7	Siltstone mixed with mudstone debris	139.0	32.6	19.1	1.71	1.01	3.38	2.47	442	137	40.9	0.04	1.94	2.15	448	90
1963.7	Organic-lean lamina	102.7	44.4	17.0	2.61	3.74	24.77	9.49	447	261	39.4	0.21	21.26	9.18	453	232
1963.7	Organic-rich lamina	33.7	30.0	26.3	1.14	5.91	43.14	23.1	443	187	25.6	0.22	39.14	23.82	442	164

3. Results and discussion

3.1. Profile of hydrocarbon expulsion or retention

The EOM and Rock-Eval analysis results for the unextracted and extracted samples are listed in Table 1. The Tmax-HI diagram (Fig. 2a) of the extracted shale samples reveals that the organic matter is thermally mature and within the hydrocarbon generation stage. According to the previously proposed Tmax–%Ro equations (Jarvie et al., 2001; Wust et al., 2012; Mastalerz et al., 2015; Evenick, 2021; Lohr and Hackley, 2021), the equivalent %Ro of the organic-rich shale samples are in the range of 0.7%–0.9%, and thus within the oil window (Table 2). In our previous study involving non-hydrous semi-open pyrolysis experiments on the Chang 7 shale, which is from the same layer as the present samples, the kerogen experienced the most intense bond-breaking reactions at 0.7%–1.0%Ro, which would thus directly result in a peak hydrocarbon generation (Ma et al., 2019; Hou et al., 2020).

Compared with organic-rich lithofacies shales, although the TOC of the organic-lean lithofacies is lower, the TOC-normalized concentrations of retained oil (S1/TOC × 100 and EOM/TOC × 100) and HI of the rocks are higher. In addition, all the FID pyrograms of the unextracted organic-lean sandstones demonstrate bimodal S2 peak, exhibiting obvious responses in the 350–450 °C range (Fig. 2b). The bimodal S2 is the result of the heavier components in the S1 not being liberated at the lower temperatures, and thus carried over into the S2 peak. The carry-over oil was confirmed to be the heavy components of the migrated oil (Clementz, 1979; King et al., 2015). Therefore, it is considered that the EOM of the siltstones are mainly introduced from the juxtaposed organic-rich shales. Affected by carry-over effect, the Tmax values are clearly suppressed. After solvent extraction, the TOC of the sandstones are reduced by more than 40%, the S_2 values are decreased by more than 70%, the HI values are decreased by more than 65%, and the Tmax values shift 7–32 °C toward higher temperature. For organic-rich shales, before and after solvent extraction, the changes in TOC, S_2, HI, and Tmax are much lower than those of the siltstones.

Under microscope, the organic-lean lithofacies are extensively saturated with oil (Fig. 3a-c). The in-migrated oils are presented as yellow to brown fluorescent hydrocarbons absorbed on the mineral surfaces, yellow to blue fluorescent inclusions inside the cracks of mineral grains, and non-fluorescent solid bitumen in dissolved pores (Fig. 3b). Some of the solid bitumen show bright gray reflectance under reflected white light (Fig. 3c). Raman spectroscopy was conducted on the high gray reflecting substances, and the spectra exhibit two distinct Raman bands for organic matter: disordered (D) and graphite (G) bands (the detailed analytical practices of Raman spectroscopy are reviewed in Henry et al., 2019) (Fig. 4a, b). As the microscopically observed solid bitumen are only partially dissolved, the remaining generative potentials (HI and S_2) of the sandstone may be largely attributed to the insoluble components of solid bitumen (Hackley and Cardott, 2016; Mastalerz et al., 2018).

At micro lamina-scale, the relatively organic-lean lamina also exhibits (1) higher TOC-normalized EOM, and (2) obvious Tmax right shift after extraction. Different from that of the organic-lean lithofacies rocks, the TOC of the organic-lean lamina was still as high as 9.18%, even after organic solvent extraction. We infer that the remaining generation potentials detected in silty lamina are contributed by nonvolatile solid bitumen, which is also the solid residue of degraded liquid hydrocarbons generated by and in migrated from the organic-rich lamina.

Table 2
%Ro–Tmax equations and calculated minimum and maximum vitrinite reflectance.

Reference	Equation	Tmax (°C) min	Tmax (°C) max	%Ro min	%Ro max
Jarvie et al., 2001	%Ro(Tmax) = 0.018 × (Tmax) − 7.16	440	445	0.76	0.85
Wust et al., 2012	%Ro(Tmax) = 0.0149 × (Tmax) − 5.85	440	445	0.71	0.79
Mastalerz et al., 2015	%Ro(Tmax) = 0.0151 × (Tmax) −5.9127	440	445	0.73	0.81
Evenick, 2021	%Ro(Tmax) = 0.013 × (Tmax) − 5.0	440	445	0.72	0.78
Lohr and Hackley, 2021	%Ro(Tmax) = 0.0317 × (Tmax) − 13.224	440	445	0.72	0.88

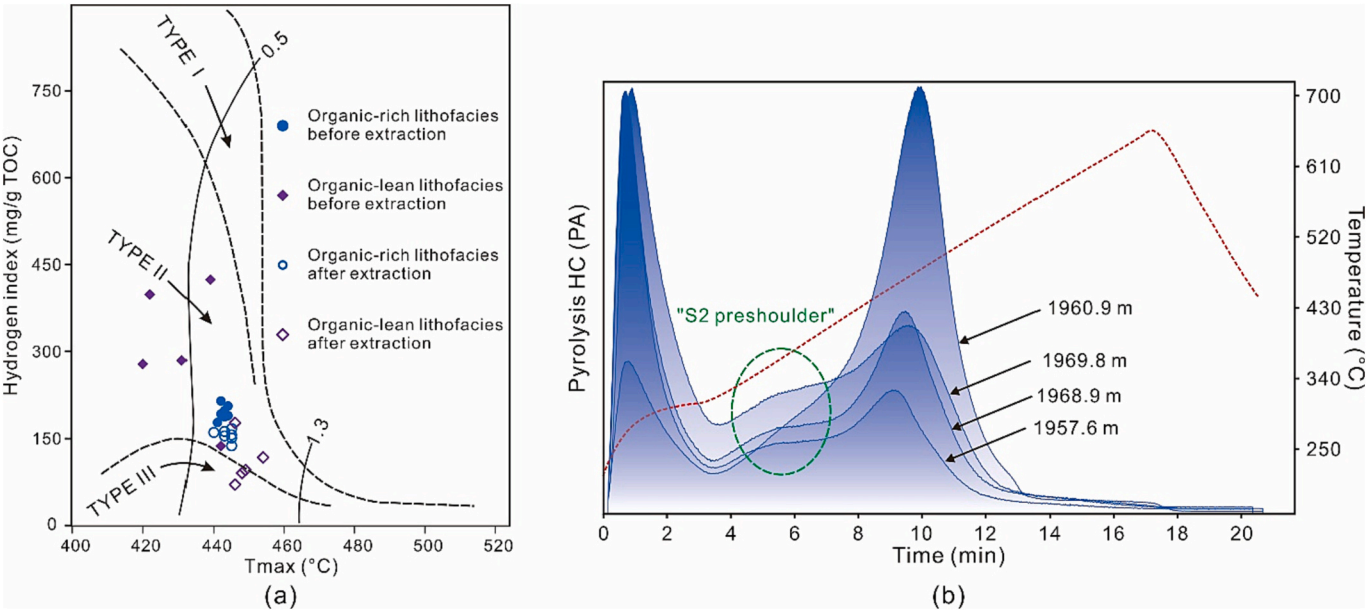

Fig. 2. (a) Tmax-HI diagram of the rock samples before and after solvent extraction. (b) Rock-Eval flame ionization detector (FID) pyrogram of organic-lean rock samples. Note: the red curve in (b) records the temperature of the inlet rod of the sample crucible. (For interpretation of the references to colour in this figure legend, the reader is referred to the web version of this article.)

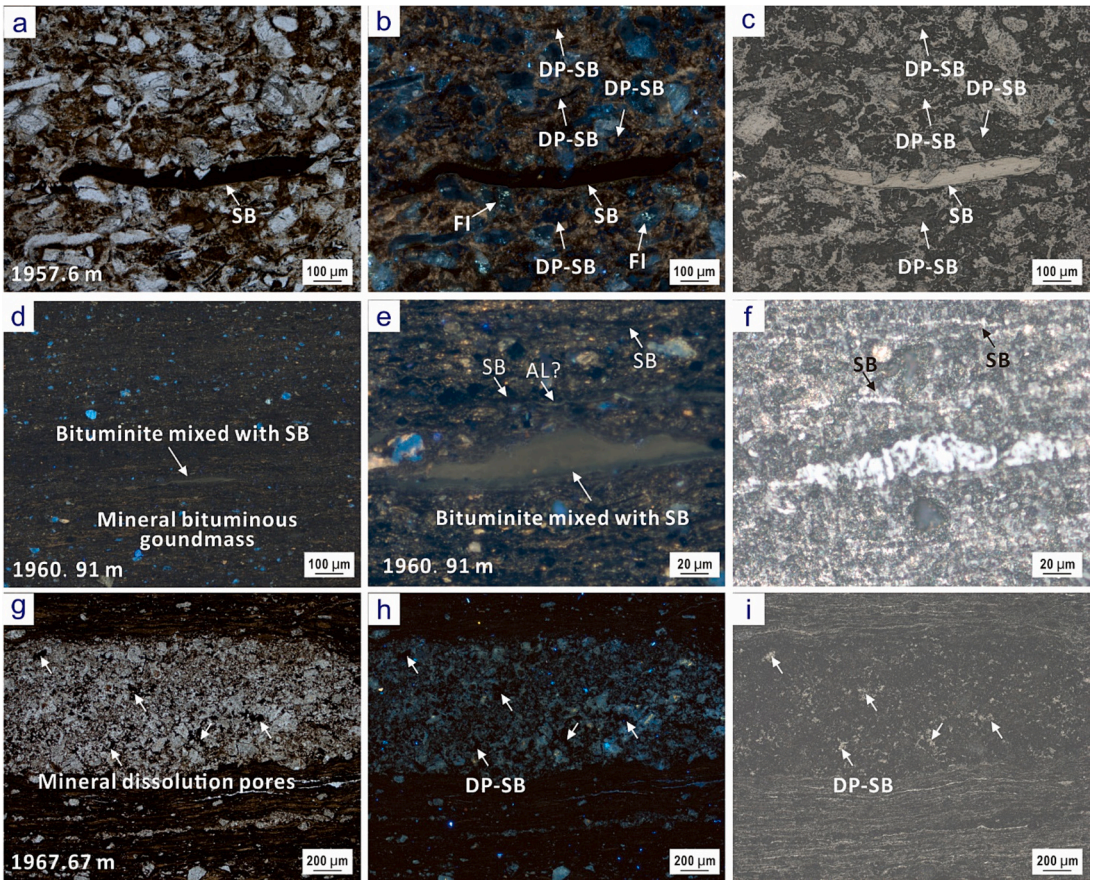

Fig. 3. Petrographic images of organic matter occurrence in interbedded siltstone (a-c), organic-rich lamina (d-f), and silty lamina (g-i). (a) Thin section photomicrograph (plane-polarized) showing embayment texture of solid bitumen by euhedral mineral crystal terminations (b) Same view as (a) under UV showing dissolution pores filled with solid bitumen (DP-SB), and yellow-blue fluorescent hydrocarbon fluid inclusions (FI). The pale brown fluorescent material may be hydrocarbons absorbed by clay minerals. (c) Same view as (a, b) under reflected light (dry objective), the white arrows are at the same position as in (b). (d) Thin section photomicrograph (ultraviolet fluorescence, UV) showing "schlieren" bituminite and thermal conversion product solid bitumen (SB) in matrix of fluorescent mineral bituminous groundmass. (e) Thin section photomicrograph (ultraviolet fluorescence, UV) showing close view of bituminite mixed with solid bitumen, solid bitumen (SB), and suspected alginite (AL). Solid bitumen presents as long strip. (f) Same view as (e) under reflected light (dry objective). (g) Thin section photomicrograph (plane-polarized) showing mineral dissolution pores (DP) in silty lamina. (h) Same view as (g) under UV showing dissolution pores filled with solid bitumen (DP-SB). Solid bitumen presents as block-like aggregates. (i) Same view as (g, h) under reflected light (dry objective), the white arrows are at the same position as in (e). (For interpretation of the references to colour in this figure legend, the reader is referred to the web version of this article.)

In organic-rich lamina within shale, the organic matter is mainly composed mineral bituminous groundmass (Fig. 3 d-f). Under fluorescent, "schlieren" bituminite, occurring as elongated stringers, dark yellow suspected alginite and non-fluorescent elongated solid bitumen streaks are dispersed in mineral bituminous groundmass (Fig. 3e). The dark brown or non-fluorescent elongated streaks, which are in close proximity to the yellow suspected alginite, exhibit bright gray reflectance under white reflected light (Fig. 3f). This observation may suggest the in-situ conversion of alginite to solid bitumen. In microscale reservoir, i.e., organic-lean lamina within shale, mineral dissolution pores are common (Fig. 3g). Organic matter is mainly presented as solid bitumen filling dissolution pores (Fig. 3h, i and Fig. 4c, d). Solid bitumen in organic-lean lamina occurs as block-like aggregates, obvious different from that in organic-rich lamina, in which solid bitumen mainly occurs as long strips. Therefore, the organic matter in the organic-lean lamina is most likely remobilized oil residue that generated and migrated from organic-rich lamina, and then accumulated in dissolution pores, instead of generated in-situ. In the previous study (Ma et al., 2022), we characterized the occurrence of organic matter under microscope in a low thermal matured shale that is also comprised of organic-rich lamina and organic-lean lamina. Microscopically, primary macerals are rarely observed in the organic-lean lamina, further confirming that the organic matter in it was not indigenously generated. The silty lamina in the low thermal matured shale samples have the same sedimentogenesis with the thermal matured shale samples in this study. Therefore, we infer that the silty lamina mainly received oil from the interlaminated organic-rich lamina, similar to the lithofacies shale and (silt-) sandstone pairs.

3.2. Composition of EOM in source rock and reservoir lithofacies

3.2.1. Bulk composition

The relative proportions of the saturated fractions and the saturates/aromatics (S/A) ratios in the organic-lean lithofacies and lamina are consistently greater than those in the organic-rich counterparts (Table 1). This chemical fractionation effect of preferential expulsion and migration saturates over aromatics has been verified both in the field and in laboratory experiments (e.g., Sandvik et al., 1992; Han et al., 2015). The 1958.5–1966.5 m interval is thick shale lithofacies. From the center to the edge of this interval, the TOC–normalized EOM show a decreasing trend, which indicates that the edges of the source rock may have expelled more oil than the middle. A similar enhanced expulsion effect toward the reservoir lithofacies was noted more than thirty years ago by Leythaeuser et al. (1988). Because the edges of the thick shale interval expelled more oil, more saturates may be expelled as well, as revealed by lower saturated fraction proportion and S/A ratio. In addition, in the lower interval below 1965 m, thin shale source rocks are

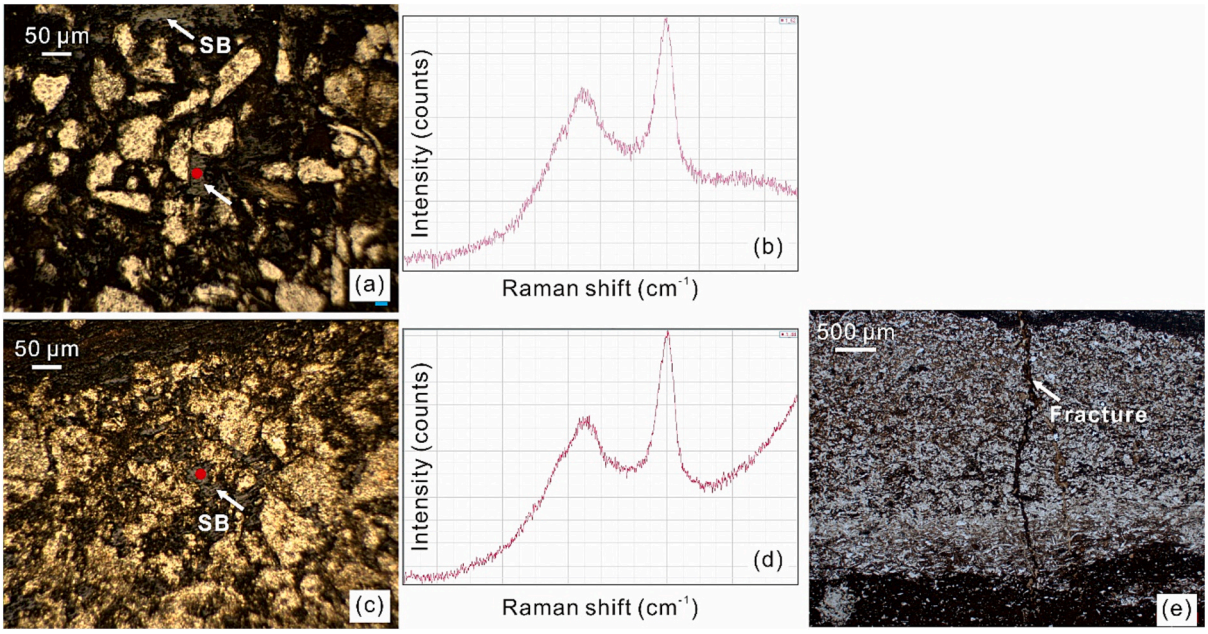

Fig. 4. Raman spectroscopy of solid bitumen in siltstone and organic-lean silty lamina (a-d), and solid bitumen filled fracture (e). (a) Photomicrograph shot by the microscope matched with Raman spectroscopy (partial plane-polarized and partial reflected light) showing (SB, white arrows) and measuring point (red dot) of Raman spectra, C30 1969.8 m, siltstone. (b) Raman spectrum of the test point in (a). (c) Photomicrograph shot by the microscope matched with Raman spectroscopy (partial plane-polarized and partial reflected light) showing (SB, white arrows) and measuring point (red dot) of Raman spectra, C30 1967.7 m, organic-lean lamina in shale. (d) Raman spectrum of the test point in (c). (e) Thin-section photomicrograph (plane-polarized) showing fracture filled with SB, C30 1963.7 m, organic-lean lamina in shale. (For interpretation of the references to colour in this figure legend, the reader is referred to the web version of this article.)

interbedded with siltstone reservoirs, and silty laminae are very abundant within single shale lithofacies. Such lithofacies characteristics provide favorable conditions for the expulsion and migration of oil into the interlaminated silty lamina or interbedded sandstone. This also illustrates that a meter-scale source-reservoir lithofacies stacking pattern is beneficial for oil migration, as demonstrated by Zhang et al. (2021). As a result, the relative concentration of saturates and the S/A ratios in the lower thin shale interval are generally lower than the upper thick shale interval.

3.2.2. *Molecular composition*

Compared with the undisputable understanding on chemical fractionation of preferential expulsion and migration saturates over aromatics described above, the molecular fractionation of C_{15+} *n*-alkanes remains highly controversial. Mishra et al. (1996) used a hydrous pyrolysis experiment together with a stepwise extraction technique and found that short chain *n*-alkanes migrate or expel more easily than long chain ones. Their study used the same organic solvent, but different sample sizes. Similar results were obtained by Pan et al. (2002), who also used multi-step extraction method, but based on different organic solvent. However, the conclusions derived from these experiments are inconsistent with field observations. Some studies observed no evidence for expulsion fractionation, and authors concluded that oil was pressure-driven and expelled as single-phase liquid (Leythaeuser et al., 1988; Wilhelms et al., 1990; Eseme et al., 2007). Other studies found that higher-molecular-weight (HMW) *n*-alkanes were more intensely expelled when the source rocks were type-III kerogen and the oil was expelled by dissolution in a gas phase (Leythaeuser et al., 1984, 1988). Some recent studies also found that lower-molecular-weight (LMW) *n*-alkanes were enriched in the organic-rich source-rock interval (Han et al., 2015; Zou et al., 2019).

In this study, at lithofacies-scale, higher $\sum C_{21-}/\sum C_{22+}$ ratios were observed in the organic-rich source-rock lithofacies, and such result is similar to Han et al. (2015) and Zou et al. (2019) (Fig. 5a). However, at lamina-scale, a higher $\sum C_{21-}/\sum C_{22+}$ ratio was observed in the silty lamina. Han et al. (2015) ascribed the lithofacies-scale higher $\sum C_{21-}/\sum C_{22+}$ ratios in reservoir to phase separation. According to Han et al. (2015), fractures develop in the oil-received interval. During the opening of the fracture, a sudden pressure decrease caused phase separation, which selectively transfers lower molecular weight hydrocarbons into the vapor phase, leaving the heavy-end liquid phase remaining in the respective interval (Larter and Mills, 1991). Phase separation is not a favorable explanation in the present study, because it cannot explain the contradictory $\sum C_{21-}/\sum C_{22+}$ ratio at lamina scale. In the organic-lean oil-received lamina, fractures are common (Fig. 4e). However, the silty lamina still has higher proportion of $\sum C_{21-}$. In the work of Jarvie (2014), he found that during sample handling, the evaporative loss of light hydrocarbon in the organic-lean rock is more intense than that in the organic-rich rock. Because of relatively low TOC content, the absorption capability of reservoir rock is weaker than that of source rock. In addition, the porosity and permeability of reservoir rock is higher than that of the source rock. Therefore, during sample crushing and EOM extracting, the reservoir rock lost much more volatile light hydrocarbons than source rocks. Light hydrocarbon evaporative loss effect can explain the higher $\sum C_{21-}/\sum C_{22+}$ ratio in the organic-rich source-rock lithofacies, but cannot explain the lower $\sum C_{21-}/\sum C_{22+}$ ratio in the organic-rich lamina. Because both organic-rich shale and lamina have higher TOC and poor reservoir quality than their organic-lean counterparts. However, the total ion chromatogram (TIC) of the saturated fraction in GC–MS analysis shows identical *n*-alkane distribution range between organic-rich lamina and organic-lean lamina (Fig. 6a, c). In addition, the n-C_{14} and n-C_{15} peak of the silty lamina is obviously higher than that of organic-rich silty lamina.

In the present circumstances, we envisage a scenario in which LMW *n*-alkanes do indeed migrate more rapidly than HMW *n*-alkanes, as revealed by the distribution pattern between the micro source rock and reservoir assemblage. The seemingly inconsistent distribution pattern of *n*-alkanes in the organic-lean lithofacies may be caused by different degree of oil maturity. According to our previous study, the micro reservoir, i.e., silty lamina, has the privilege to accumulate the

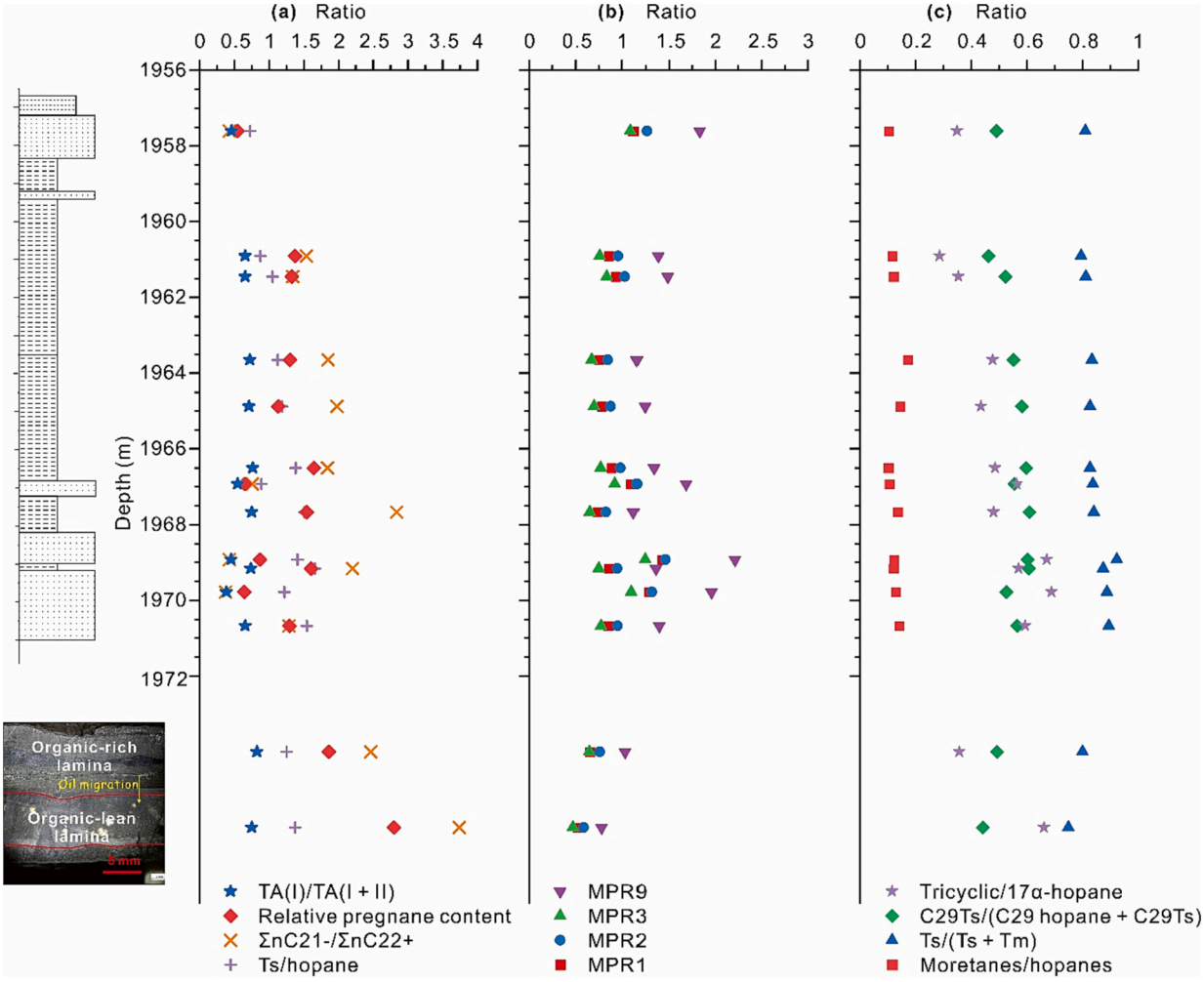

Fig. 5. Profile of thermal maturity-related parameters. The abbreviations and calculation method were presented in the Appendix. Note that in order to make the trend more obvious, Ts/hopane was multiplied by 2.

generated products from the immediately adjacent organic-rich lamina (Ma et al., 2022). Because of the strong storage capacity of silty lamina within lithofacies-scale source rock (shale), fluids are less readily to expel out to lithofacies-scale reservoir (sandstone). As a result, the organic-lean lithofacies reservoirs are less readily to receive the newly generated and more mature hydrocarbons from the adjacent shales, resulting in low $\sum C_{21-}/\sum C_{22+}$ ratio that reflects early expelled hydrocarbons with low thermal maturity chemical signature. The peak heights of C_{22+} *n*-alkaness in the muddy siltstone are clearly higher than that of shale (Fig. 6b, d).

The above inference can be supported by other molecular indicators (Fig. 5a); please see appendix A1 for the detailed calculation method. From the distribution of the biomarker parameters between the source rock and the reservoir, the relative C_{21} and C_{22} sterane content (also called relative pregnane content) and Ts/hopane parallel with $\sum C_{21-}/\sum C_{22+}$ at both lamina and lithofacies scales (Fig. 5a). On a chemical basis, the concentrations of three index-related compounds are synchronized with oil generation, and they partially share the same precursor–products reaction mechanism. Specifically, in addition to being directly released from the kerogen structure, lower-molecular-weight (LMW) hydrocarbons can be generated by thermal cracking of higher-molecular-weight (HMW) hydrocarbons (Hill et al., 2003), C_{21} sterane (pregnane) and C_{22} sterane (homopregnane) can be generated by the side-chain cleavage of regular steranes (Huang et al., 1994), and Ts is believed to be generated by side-chain cleavage and rearrangement of C_{29} and higher-carbon-number hopanoids (Volkman et al., 1983). Additionally, the migration efficiency of pregnane and homopregnane is greater than that of regular steranes. The studied samples are in the intense oil generation stage and would thus progressively expel more mature oil. However, due to the strong storage capacity of the silty lamina within the organic-rich source-rock lithofacies, the organic-poor reservoir lithofacies was unable to receive the latest generated mature oils. Therefore, the oils in interbedded organic-lean lithofacies are most likely early-expelled products. As the oils in the reservoir are believed to be less prone to thermal alteration than those in the source rock (Cornford et al., 1986; Peters et al., 2005), they carry a lower thermal maturity chemical signature. The profile in which the organic-lean reservoirs possess lower thermal mature biomarkers compared with the adjacent organic-rich source rocks was also observed by Tang et al. (2018) in a lacustrine marlstone succession. Another noticeable biomarker indicator is the variation of TA(I)/TA(I + II) in aromatics (Fig. 5a); it has the same chemical basis and lithofacies-scale variation trend as the above-mentioned saturated biomarkers, and the only difference is that it does not show fractionation at the lamina scale. Maybe due to the same generation mechanism of direct side-chain cleavage precursor–products relationship, any two parameters in relative pregnane content, $\sum C_{21-}/\sum C_{22+}$, and TA(I)/TA(I + II) share good positive correlations (Fig. 7).

It is worth mentioning that when analyzing maturity-related indices, we found that there are also regular variations in the distribution of the phenanthrene (P) and methylphenanthrene (MP) related parameters, but the change trends were exactly opposite to those of $\sum C_{21-}/\sum C_{22+}$

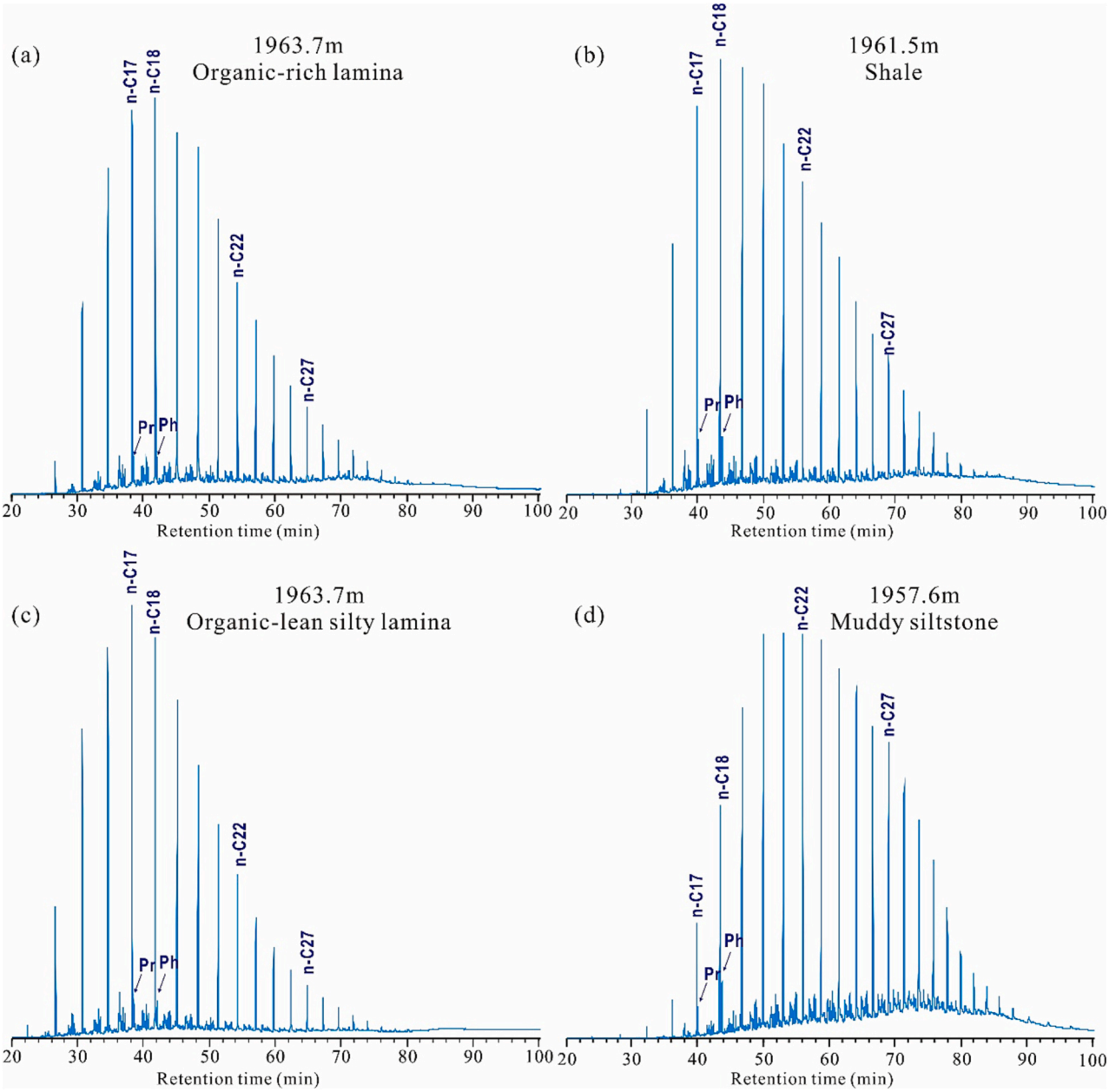

Fig. 6. Total ion chromatogram (TIC) of the saturated fraction of gas chromatography–mass spectrometry (GC–MS) analysis showing the distribution of *n*-alkanes in EOM.

and the relative pregnane content (Fig. 5b). At lamina scale, the ratios of MP/P (MPR 1, 2, 3, and 9) in organic-rich lamina are higher than those in silty lamina, while at lithofacies scale, the ratios are greater in sandstones than in shales. As with the *n*-alkanes and (homo-) pregnanes, the increased abundance of phenanthrene homologous occurs simultaneously with intense hydrocarbon generation (Radke et al., 1986; Radke and Willsch, 1994; Requejo, 1994). However, their generation mechanism changes with increasing degree of thermal alteration and the fractionation effect remain indefinite conclusions (Radke et al., 1982; Radke et al., 1986; Radke, 1988). The comparatively well-supported chemical basis for the thermal maturity-driven methylation reaction of P to MP (Radke, 1988) fails to explain the lower MP/P ratios in the shales compared to siltstones. The specific reasons for this phenomenon need to be further revealed. In the present study and for the Chang 7_3 sub-member shale system, more work is needed to be done when using MP/P ratios to indicate maturity.

Some of the other commonly used thermal maturity indicators (Fig. 5c) exhibit either indistinguishable changes (such as moretanes/hopanes, Ts/(Ts + Tm), C_{29}Ts/(C_{29} hopane + C_{29}Ts)) or unsystematic variations (such as tricyclics/17α-hopanes). The chemical basis for these thermal maturity parameters is isomerization reaction or selective loss of unstable homologs or epimers. The ratio of moretanes/hopanes would be balanced at early oil generation stage, and that tricyclics/17α-hopanes was less specific after thermal mature stage.

Therefore, we conclude that specific reactions, such as those involving chain scission reactions, are very sensitive to the reaction environments in source rocks and reservoirs. This results in thermal cracking of specific compounds, which further results in the chain breaking-induced maturity-related parameters showing obvious differences, even within the short interval of a shale system where differences in thermal maturity were not expected. Need to mention that, although thermal maturity of these shales is overall about 0.9%, the retained oil in these shales has been cracked to a considerable content. According to pyrolysis experiment, the kerogen decomposition of the Chang 7 shale is

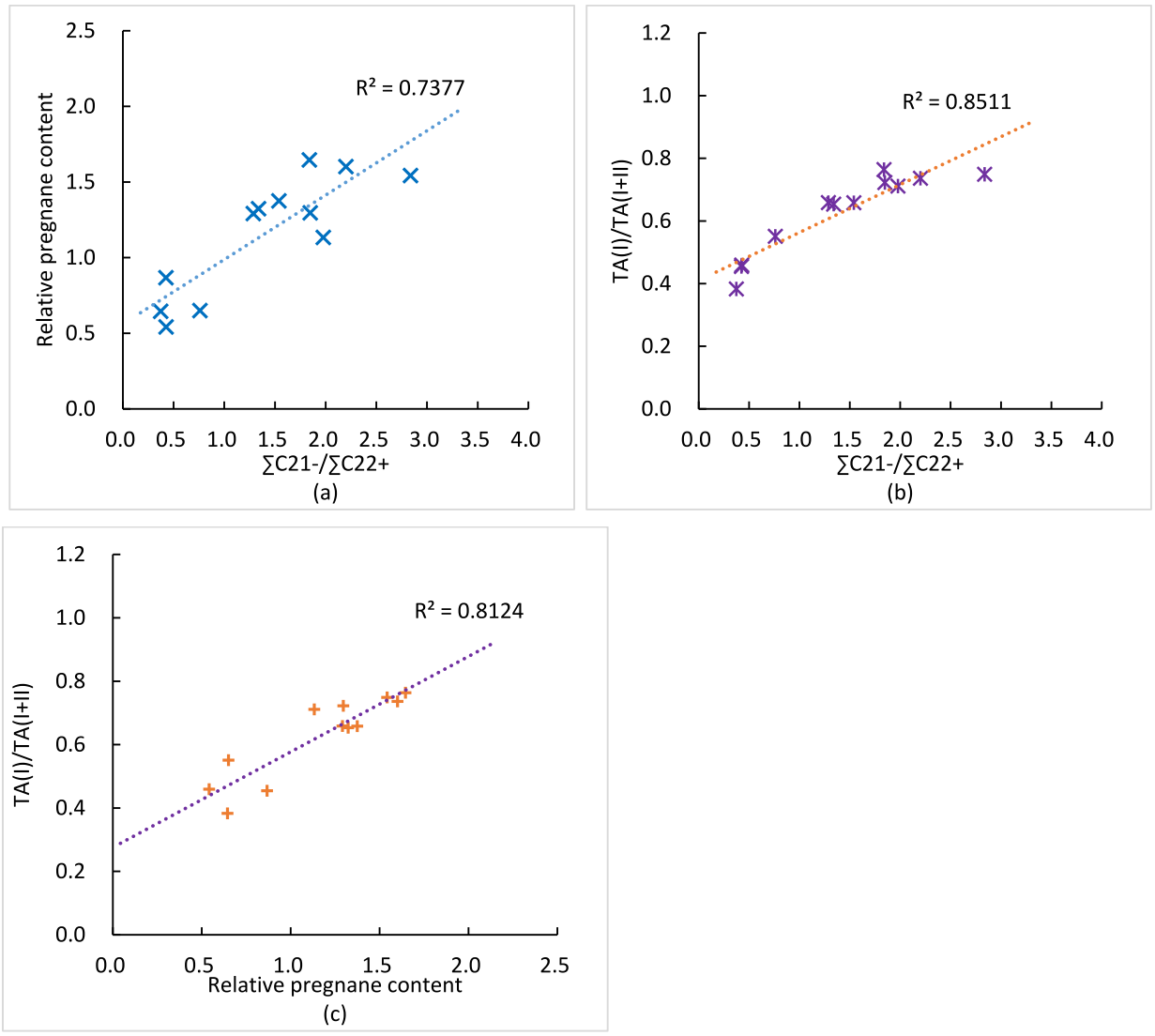

Fig. 7. Positive linear correlations between (a) $\sum C_{21-}/\sum C_{22+}$ vs. relative pregnane content, (b) $\sum C_{21-}/\sum C_{22+}$ vs. TA(I)/TA(I + II), and (c) relative pregnane content vs. TA(I)/TA(I + II).

accompanied by cracking of C_{15+} fractions. After about 1.1% Ro, the rate of oil cracking exceeds that of oil generation (Ma et al., 2020).

Coincidentally, The difference in molecular composition between organic-rich and organic-lean lithofacies is similar to the Rock-Eval Tmax. As we have mentioned in section 3.1, the Tmax of organic-lean reservoir samples before solvent extraction is lower than that of organic-rich source rock samples. The three parameters $\sum C_{21-}/\sum C_{22+}$, relative pregnane content, and TA(I)/TA(I + II) of the organic-lean reservoir samples are also relatively smaller than that of organic-rich source rock samples. Therefore, in the correlation figure of Tmax vs. molecular parameter, the organic-lean and organic-rich lithofacies were separated (Fig. 8).

It should be noted that, comparisons of the bulk and molecular composition were only made between source rock and reservoir at the same scale. The EOM composition of the lithofacies-scale source rock cannot be compared with that of the lamina-scale source rock, and the EOM composition of the lithofacies-scale reservoir cannot be compared with that of the lamina-scale reservoir, either. This is because the rock samples and the microdrilled samples were extracted by different method, as described in section 2.2. The temperature, pressure, and duration extraction are different between ASE and ultrasonic extraction. Therefore, there should be differences in the absolute yield and chemical composition of EOM obtained by the two methods. This defect needs to be improved in the future work.

3.3. *The effect of hydrocarbon expulsion on the thermal evolution of EOM*

The molecular composition of EOM is not only influenced by the lithofacies, as discussed above, but also affected by the lithofacies assemblage. In the profile of the molecular composition variations (Fig. 5a), the $\sum C_{21-}/\sum C_{22+}$, Ts/hopane, relative pregnane content, and TA(I)/TA(I + II) in the shale interval below 1966.5 m were generally greater than those in shale intervals above 1966.5 m. The lithofacies below 1966.5 m is thin layers of interbedded silt-to sandstone and shale. As discussed in Section 3.2.1, proximity to reservoir enables the oil in the shale rock more easily to expel out. Therefore, from the higher proportion of chain breaking products $\sum C_{21-}$, Ts, $C_{21} + C_{22}$ sterane, and TA(I) compared to their precursors, it is reasonable to infer that oil expulsion promotes further chain breaking reaction of the oil retained in the source rocks.

Many studies have been conducted to investigate the impact of retention or expulsion on oil and gas generation from kerogen decomposition. Burnham and McConaghy (2014) demonstrated that hydrocarbon expulsion increases the yield of oil and gas. Wu et al. (2019)

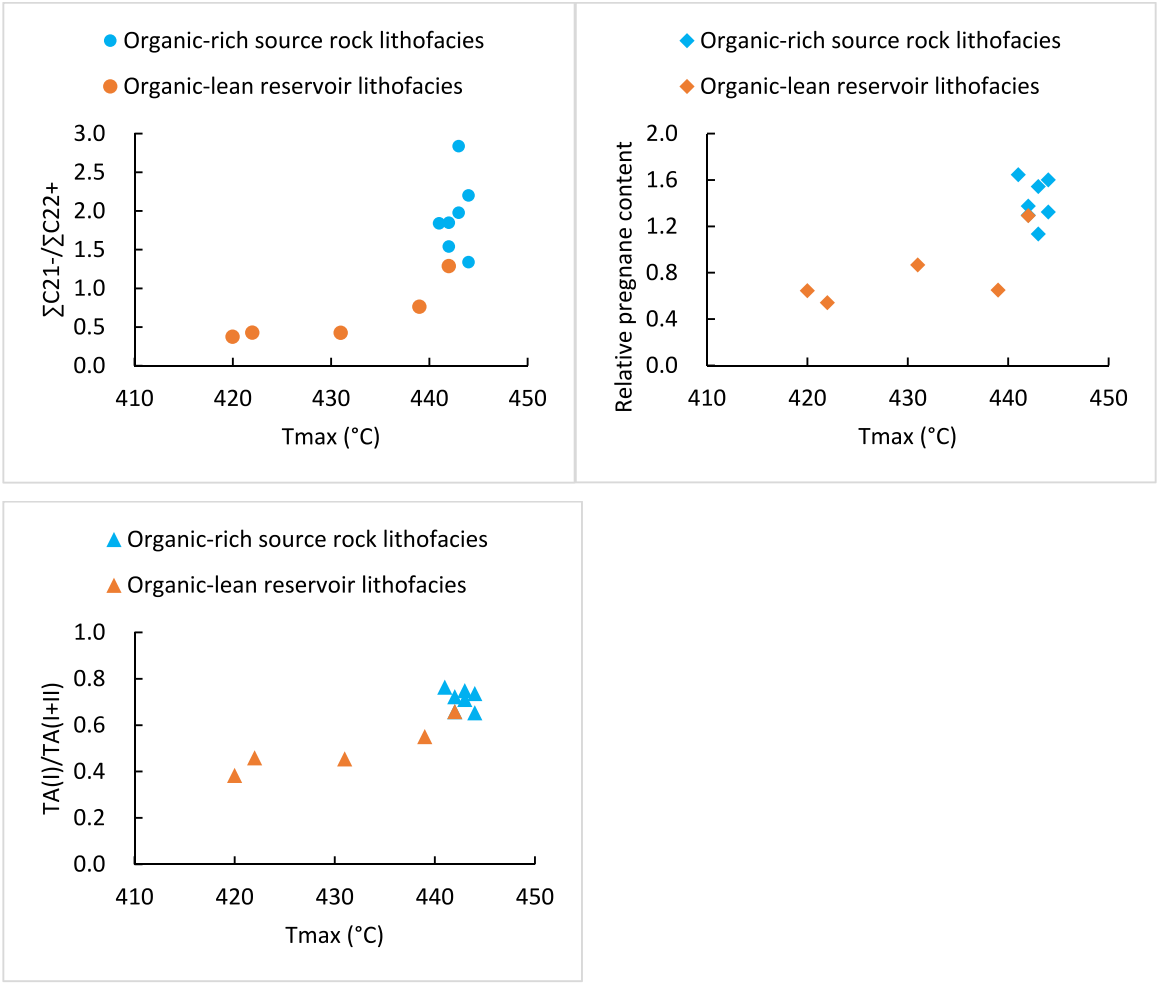

Fig. 8. Variations in Tmax and chain breaking reaction-related thermal maturity indices within source rocks and reservoir lithofacies.

suggested that oil expulsion promotes long chain cracking within kerogen. Carr (1999) found that prevention of oil expulsion during maturation retards further kerogen maturation. In the present study, similar result was obtained for secondary cracking of retained oil. Because the kerogen decomposition and oil cracking occur simultaneously over a period of time, we speculate that hydrocarbon expulsion will promote both secondary cracking of oil and subsequently kerogen decomposition, because the two processes are an inherited continuous process, as Carr (1999) proposed that retention of reaction products in the structures of the organic matter would suppress the rate of further maturation reaction.

It has been concluded that shale system with frequent stacking assemblages of source rock and reservoir is an ideal target for shale oil exploration, because it (1) provides conduits or spaces for oil migration and storage, (2) is more easily to be fractured and thus simple production characteristics (Jarvie, 2012; Zhang et al., 2021). In addition to the above-mentioned reasons, we assume that the enhanced thermal evolution of shale oil caused by hydrocarbon expulsion may be another reason to explain why source-reservoir lithology stacking assemblages provide good conditions for the development of shale oil.

4. Conclusions

In this study, the effect of the lamina and lithofacies assemblage within a typical hybrid shale system and the associated assemblage–induced hydrocarbon expulsion differences on the molecular composition of EOM were discussed. Chemical fractionation, preferential migration and expulsion of saturate fraction occurs at both lithofacies and lamina-scale source rock–reservoir assemblages. Molecular fractionation, preferential expulsion of LMW *n*-alkanes occurs at lamina-scale source rock-reservoir assemblages. At lithofacies scale, due to the strong storage capacity of the laminated micro reservoir within shale, the lithofacies-scale reservoir cannot receive the newly generated oil, and thus it exhibits low thermal maturity signature and have a lower $\sum C_{21-}/\sum C_{22+}$.

Chain scission reactions of oil are very sensitive to the reaction environments in source rocks and reservoirs. This results in the chain breaking-induced maturity-related parameters such as $\sum C_{21-}/\sum C_{22+}$, relative pregnane content, Ts/hopane and TA(I)/TA(I + II) being lower in the reservoir lithofacies even within a short interval of a shale system.

In a shale system where interbedded organic-lean lithofacies is developed, oil in the organic-rich lithofacies is more easily to be expelled out. Oil expulsion promotes further secondary cracking of the oil retained in the source rocks, and subsequently kerogen decomposition. This inherited continuous process provides an additional reason to explain the frequent-stacking assemblage of source rock and reservoir lithofacies as an ideal shale oil exploration target.

CRediT authorship contribution statement

Weijiao Ma: Conceptualization, Methodology, Writing – original draft, Writing – review & editing. **Yingchang Cao:** Project administration, Supervision, Conceptualization, Resources. **Kelai Xi:** Resources. **Miruo Lin:** Investigation, Resources. **Jinzhong Liu:** Funding

acquisition. **Yunpeng Wang:** Project administration, Supervision.

Declaration of Competing Interest

The authors declare that they have no known competing financial interests or personal relationships that could have appeared to influence the work reported in this paper.

Data availability

Data will be made available on request.

Acknowledgments

This work was supported by the Natural Science Foundation of China (Grant No. 42102155), State Key Laboratory of Organic Geochemistry, GIGCAS (Grant No. SKLOG202110). We thank Yong Li and Qiang Wang from the State Key Laboratory of Organic Geochemistry, Guangzhou Institute of Geochemistry, Chinese Academy of Sciences for their help during the GC–MS analysis. The editor Deolinda Flores and the two anonymous reviewer are greatly appreciated for their hard work and patience in polishing and improving this manuscript.

Appendix A. Appendix

Table A1
Compounds used to calculate thermal maturity parameters and associated calculation methods.

Parameters	Related compounds and calculation methods
Relative pregnane content	(C_{21} sterane + C_{22} sterane)/C_{27}–C_{29} ααα sterane)
Ts/hopane	C_{27}-18α-22,29,30-trisnorneohopane/C_{29}-17α(H),21β(H)-hopane
TA(I)/TA(I + II)	C_{20}–C_{21} triaromatic sterane/ (C_{20}–C_{21} triaromatic sterane + C_{26}–C_{28} triaromatic sterane)
Moretanes/hopanes	C_{30}-17β(H),21α(H)-hopane/C_{29}-17α(H),21β(H)-hopane
Ts/(Ts + Tm)	C_{27}-18α-22,29,30-trisnorneohopane/(C_{27}-18α-22,29,30-trisnorneohopane + C_{27}-17α-22,29,30-trisnorhopane)
C_{29}Ts/(C_{29} hopane + C_{29}Ts)	C_{29}-18α,21β-30-norneohopane/(C_{29}-18α,21β-30-norneohopane + C_{29}-17α,21β-30-norhopane)
Tricyclics/17α-hopanes	C_{28}-C_{29} (S + R) tricyclic terpane/C_{29}–C_{33} 17α-hopanes
MPR1	1-Methylphenanthrene/Phenanthrene
MPR2	2-Methylphenanthrene/Phenanthrene
MPR3	3-Methylphenanthrene/Phenanthrene
MPR9	9-Methylphenanthrene/Phenanthrene

References

Behar, F., Beaumont, V., Penteado, H.L.D., 2001. Rock-Eval 6 technology: Performances and developments. Oil Gas Sci. Technol. 56, 111–134.

Burnham, A.K., McConaghy, J.R., 2014. Semi-open pyrolysis of oil shale from the garden gulch member of the Green River formation. Energy&Fuels 28, 7426–7439.

Carr, A.D., 1999. A vitrinite reflectance kinetic model incorporating overpressure retardation. Mar. Pet. Geol. 16, 355–377.

Chen, Y., Mastalerz, M., Schimmelmann, A., 2012. Characterization of chemical functional groups in macerals across different coal ranks via micro-FTIR spectroscopy. Int. J. Coal Geol. 104, 22–33.

Chukwuma, K., Tsikos, Harilaos, Wagner, N., 2021. Control of variability of primary grain assemblages on the stratigraphicmdifferences in diagenetic processes and products inorganic-rich sediments. Sediment. Geol. 422, 105966.

Clementz, D.M., 1979. Effect of oil and bitumen saturation on source-rock pyrolysis. AAPG Bull. 63, 2227–2232.

Cornford, C., Needham, C.E.J., de Walque, L., 1986. Geochemical habitat of North Sea oils. In: Spencer, A.M. (Ed.), Habitat of Hydrocarbons on the Norwegian Continental Shelf. Graham and Trotman, London, pp. 39–54.

Eseme, E., Littke, R., Krooss, B.M., Schwarzbauer, J., 2007. Experimental investigation of the compositional variation of petroleum during primary migration. Org. Geochem. 38, 1373–1397.

Espitalié, J., Madec, M., Tissot, B., Mennig, J., Leplat, P., 1977. Source rock characterization method for petroleum exploration. In: The 9th Annual Offshore Technology Conference. Offshore Technology Conference, Houston, Texas, pp. 439–444.

Evenick, J.C., 2021. Examining the relationship between Tmax and vitrinite reflectance: an empirical comparison between thermal maturity indicators. J. Nat. Gas Sci. Eng. 91, 103946.

Hackley, P.C., Cardott, B.J., 2016. Application of organic petrography in north american shale petroleum systems: a review. Int. J. Coal Geol. 163, 8–51.

Hackley, P.C., Lünsdorf, N.K., 2018. Application of Raman spectroscopy as thermal maturity probe in shale petroleum systems: insights from natural and artificial maturation sequences. Energy&Fuel 32, 11190–11202.

Han, Y., Mahlstedt, N., Horsfield, B., 2015. The Barnett Shale: Compositional fractionation associated with intraformational petroleum migration, retention, and expulsion. AAPG Bull. 99, 2173–2202.

Henry, D.G., Jarvis, I., Gillmore, G., Stephenson, M., 2019. Raman spectroscopy as a tool to determine the thermal maturity of organic matter: Application to sedimentary, metamorphic and structural geology. Earth Sci. Rev. 198, 102936.

Hill, R.J., Tang, Y., Kaplan, I.R., 2003. Insights into oil cracking based on laboratory experiments. Org. Geochem. 34, 1651–1672.

Hou, L., Ma, W., Luo, X., Tao, S., Guan, P., Liu, J., 2020. Chemical structure changes of lacustrine Type-II kerogen under semi-open pyrolysis as investigated by solid-state ^{13}C NMR and FT-IR spectroscopy. Mar. Pet. Geol. 116, 104348.

Huang, D., Zhang, D., Li, J., 1994. The origin of 4-methyl steranes and pregnanes from Tertiary strata in the Qaidam Basin, China. Org. Geochem. 22, 343–348.

Jarvie, D.M., 2012. Shale Resource Systems for Oil and Gas: Part 2—Shale-oil Resource Systems. In: Breyer, J.A. (Ed.), Shale Reservoirs—Giant Resources for the 21st Century, AAPG Memoir, vol. 97, pp. 89–119.

Jarvie, D.M., 2014. Components and Processes Affecting Producibility and Commerciality of Shale Resource Systems. Geol. Acta 12, 307–325.

Jarvie, D., Claxton, B., Henk, F., Breyer, J., 2001. Oil and Shale Gas from the Barnett Shale. In: AAPG National Convention. Denver, Ft. Worth Basin, Texas.

Jubb, A.M., Botterell, P.J., Birdwell, J.E., Burruss, R.C., Hackley, P.C., Valentine, B.J., Hatcherian, J.J., Wilson, S.A., 2018. High Microscale Variability in Raman thermal Maturity estimates from Shale Organic Matter. Int. J. Coal Geol. 199, 1–9.

Kelemen, S.R., Afeworki, M., Gorbaty, M.I., Sansone, M., Kwiatek, P.J., Walters, C.C., Freund, H., Siskin, M., 2007. Direct characterization of kerogen by X-ray and solid-state 13C nuclear magnetic resonance methods. Energy Fuel 21, 1548–1561.

King, R.R., Jarvie, D., Cannon, D., Smith, T.R., Weldon, D., Maende, A., 2015. Addressing the Caveats of Source Rock Pyrolysis in the Unconventional World: Modified Methods and Interpretative Ideas. In: Unconventional Resources Technology Conference, San Antonio, Texas, 20–22 July 2015. Society of Exploration Geophysicists, American Association of Petroleum Geologists. Society of Petroleum Engineers, pp. 919–934.

Knapp, L.J., McMillan, J.M., Harris, N.B., 2017. A depositional model for organic-rich Duvernay Formation mudstones. Sediment. Geol. 347, 160–182.

Larter, S., Mills, N., 1991. Phase-controlled molecular fractionations in migrating petroleum charges. In: England, W.A., Fleet, A.J. (Eds.), Petroleum migration: Geological Society, 59. Special Publications, London, pp. 137–147.

Leythaeuser, D., Mackenzie, A., Schaefer, R.G., Bjorøy, M., 1984. A novel approach for recognition and quantification of hydrocarbon migration effects in shale-sandstone sequences. AAPG Bull. 68, 196–219.

Leythaeuser, D., Schaefer, R.G., Radke, M., 1988. Geochemical effects of primary migration of petroleum in Kimmeridge source rocks from Brae field area, North Sea. I: Gross composition of C_{15+}-soluble organic matter and molecular composition of C_{15+}-saturated hydrocarbons. Geochim. Cosmochim. Acta 52, 701–713.

Li, M., Chen, Z., Ma, X., Cao, T., Li, Z., Jiang, Q., 2018. A numerical method for calculating total oil yield using a single routine Rock-Eval program: a case study of the Eocene Shahejie Formation in Dongying Depression, Bohai Bay Basin, China. Int. J. Coal Geol. 191, 49–65.

Lis, G.P., Mastalerz, M., Schimmelmann, A., Lewan, M.D., Stankiewicz, B.A., 2005. FTIR absorption indices for thermal maturity in comparison with vitrinite reflectance Ro in type-II kerogen from Devonian black shales. Org. Geochem. 36, 1533–1552.

Lohr, C.D., Hackley, P.C., 2021. Relating T_{max} and hydrogen index to vitrinite and solid bitumen reflectance in hydrous pyrolysis residues: Comparisons to natural thermal indices. Int. J. Coal Geol. 242, 103768.

Ma, W., Hou, L., Luo, X., Tao, S., Guan, P., Liu, J., Lin, S., 2019. Role of bitumen and NSOs during the decomposition process of a lacustrine Type-II kerogen in semi-open pyrolysis system. Fuel 260, 116211.
Ma, W., Hou, L., Luo, X., Liu, J., Tao, S., Guan, P., Cai, Yuwen, 2020. Generation and expulsion process of the Chang 7 oil shale in the Ordos Basin based on temperature-based semi-open pyrolysis: Implications for in-situ conversion process. J. Pet. Sci. Eng. 190, 107035.
Ma, W., Cao, Y., Xi, K., Liu, K., Lin, M., Liu, J., 2022. Interactions between mineral alteration and organic acids dissolved in bitumen in hybrid shale system. Submitt. Int. J. Coal Geol. 260, 104071.
Mao, J., Fang, X., Lan, Y., Schimmelmann, A., Mastalerz, M., Xu, L., Schmidt-Rohr, K., 2010. Chemical and nanometer-scale structure of kerogen and its change during thermal maturation investigated by advanced solid-state 13C NMR spectroscopy. Geochim. Cosmochim. Acta 74, 2110–2127.
Mastalerz, M., Hampton, L., Drobniak, A., 2015. Thermal Alteration Index (Tai), Vitrinite Reflectance, and Tmax through Maturation. In: 32nd Annual Meeting of the Society for Organic Petrology. Yogyakarta, Java, Indonesia.
Mastalerz, M., Drobniak, A., Stankiewicz, A.B., 2018. Origin, properties and implications of solid bitumen in source-rock reservoirs: a review. Int. J. Coal Geol. 195, 14–36.
Mishra, C.S., Samanta, U., Gupta, A., Thomas, N.J., Misra, K.N., 1996. Hydrous pyrolysis of a Type III source: fractionation effects during primary migration in natural and artificially matured samples. Org. Geochem. 25, 489–505.
Pan, C., Geng, A., Liao, Z., Xiong, Y., Fu, J., Sheng, G., 2002. Geochemical characterization of free versus asphaltene-sorbed hydrocarbons in crude oils: implications for migration-related compositional fractionations. Mar. Pet. Geol. 19, 619–632.
Peters, K.E., Walters, C.C., Moldowan, M.J., 2005. The Biomarker Guide. Cambridge University Press.
Peterson, H.I., Sanei, H., Gelin, F., Loustaunau, E., Despujols, V., 2020. Kerogen composition and maturity assessment of a solid bitumen-rich and vitrinite-lean shale: Insights from the Upper Jurassic Vaca Muerta shale, Argentina. Int. J. Coal Geol. 229, 103575.
Radke, M., 1988. Application of aromatic compounds as maturity indicators in source rocks and crude oils. Mar. Pet. Geol. 5, 224–236.
Radke, M., Willsch, H., 1994. Extractable alkyldibenzothiophenes in Posidonia Shale (Toarcian) source rocks: Relationship of yields to petroleum formation and expulsion. Geochim. Cosmochim. Acta 58, 5223–5244.
Radke, M., Welte, D.H., Willsch, H., 1982. Geochemical study on a well in the Western Canada Basin: relation of the aromatic distribution pattern to maturity of organic matter. Geochim. Cosmochim. Acta 46, 1–10.
Radke, M., Welte, D.H., Willsch, H., 1986. Maturity parameters based on aromatic hydrocarbons: influence of the organic matter type. Org. Geochem. 10, 51–63.
Requejo, A.G., 1994. Maturation of petroleum source rocks–II. Quantitative changes in extractable hydrocarbon content and composition associated with hydrocarbon generation. Org. Geochem. 21, 91–105.
Rodon, S., Littke, R., 2005. Thermal maturity in the central European Basin system (Schleswig-Holstein area): results of 1D basin modelling and new maturity maps. Int. J. Earth Sci. 94, 815–833.
Sandvik, E.I., Young, V.A., Curry, D.J., 1992. Expulsion from hydrocarbon sources: the role of organic absorption. Org. Geochem. 19, 77–87.
Tang, X., Zhang, J., Jiang, Z., Zhang, R., Lan, C., Zhao, W., Zhu, J., Wang, J., Zhao, P., 2018. Heterogeneity of organic-rich lacustrine marlstone succession and their controls to petroleum expulsion, retention, and migration: a case study in the Shulu Sag, Bohai Bay Basin, China. Mar. Pet. Geol. 96, 166–178.
Tissot, B., Pelet, R., Ungerer, P., 1987. Thermal history of sedimentary basins, maturation indices, and kinetics of oil and gas generation. AAPG Bull. 71, 1445–1466.
Volkman, J.K., Alexander, R., Kagi, R.I., Noble, R.A., Woodhouse, G.W., 1983. A geochemical reconstruction of oil generation in the Barrow Sub-basin of Western Australia. Geochim. Cosmochim. Acta 47, 2091–2106.
Wilhelms, A., Larter, S.R., Leythaeuser, D., Dypvik, H., 1990. Recognition and quantification of the effects of primary migration in a Jurassic clastic source-rock from the Norwegian continental shelf. Org. Geochem. 16, 103–113.
Wu, L., Wang, P., Geng, A., 2019. Later stage gas generation in shale gas systems based on pyrolysis in closed and semi-closed systems. Int. J. Coal Geol. 206, 80–90.
Wust, R., Hackley, P., Nassichuk, B., Willment, N., Brezovski, R., 2012. Vitrinite reflectance versus pyrolysis Tmax data: Assessing thermal maturity in shale plays with spectral reflectance to the Duvernay shale play of Western Canadian sedimentary basin. Soc. Pet. Eng. J. 167031, 1–11.
Yawar, Z., Schieber, J., 2017. On the origin of silt laminae in laminated shales. Sediment. Geol. 360, 22–34.
Zhang, T., Fu, Q., Sun, X., Hackley, P.C., 2021. Meter-scale lithofacies cycle and controls on variations in oil saturation, Wolfcamp A, Delaware and Midland Basins. AAPG Bull. 105, 1821–1846.
Zou, C., Wang, L., Li, Y., Tao, S., Hou, L., 2012. Deep-lacustrine transformation of sandy debrites into turbidites, Upper Triassic, Central China. Sediment. Geol. 265–266, 143–155.
Zou, C., Pan, S., Horsfield, B., Yang, Z., Hao, S., Liu, E., Zhang, L., 2019. Oil retention and intrasource migration in the organic-rich lacustrine Chang 7 shale of the Upper Triassic Yanchang Formation, Ordos Basin, Central China. AAPG Bull. https://doi.org/10.1306/01301917052.